PNAS
www.pnas.org

Supplementary information for:

Amyloid fibril-directed synthesis of silica core-shell nanofilaments, gels and aerogels

Yiping Cao[a], *Sreenath Bolisetty*[a], *Gianna Wolfisberg*[a], *Jozef Adamcik*[a], *and Raffaele Mezzenga*[a,b,*]

[a]ETH Zurich, Department of Health Science and Technology, Schmelzbergstrasse 9, Zurich 8092, Switzerland.
[b]ETH Zurich, Department of Materials, Wolfgang-Pauli-Strasse 10, Zurich 8093, Switzerland.

[*]Correspondence to: raffaele.mezzenga@hest.ethz.ch

Contents

www.pnas.org/cgi/doi/10.1073/pnas.1819640116

Materials and Methods

Materials. β-lactoglobulin was purified from whey protein isolated according to the previous protocol (1), provided by Davisco Foods International. Lysozyme from chicken egg white, tetraethyl orthosilicate (TEOS), acrylamide (AAm), N,N'-methylenebisacrylamide (MBA) and 2-hydroxy-4'-(2-hydroxyethoxy)-2-methylpropiophenone (UV initiator) were purchased from Sigma-Aldrich. Absolute ethanol, HCl and NaOH were from VWR International.

Preparation of amyloid fibrils. β-lactoglobulin amyloid fibrils were prepared by incubation 2 wt% protein solution at pH 2 and 90 °C for 5 h with a magnetic stirring of 300 rmp. Lysozyme amyloid fibrils were prepared at the same conditions but with a longer incubation time 24 h. During the incubation the protein monomers unfold, hydrolyze and self-assemble into amyloid fibrils. The amyloid fibrils at different pH values (pH=4, 7, 9, 12) were obtained by adjusting the pH of mature fibrils (pH=2) by 2 M NaOH. The conversion rate of protein to amyloid fibrils for β-lactoglobulin is around 82% (2). Note that the fibril concentration given in this work is the total protein concentration, including amyloid fibrils, proteins, and hydrolyzed peptides.

Fabrication of fibril-silica core-shell structures. The fibril-silica mixtures were prepared by adding varying TEOS amounts into the preformed fibrils (mature fibrils) solution with vigorous vortex 3 min. Subsequently, the samples were placed in a shaker at a speed of 400 rmp for 6 h to prevent the de-mixing of the oil-like TEOS and water-like fibril solution. The samples were used to characterization after incubation at room temperature for one week.

Preparation of aerogels. Fibril-silica composite hydrogels were solvent exchanged to ethanol with three steps by immersing in 50, 96, and 99.8 % ethanol for each one day. Next, the gels were dried by supercritical CO_2 according to the previous developed protocol (3), generating the aerogels composed of fibril-silica core-shell structures. These composite aerogels were calcined at ~700 ^{o}C for 2 h to remove the fibril core, leading to form aerogels architected by silica nanotube.

Preparation of double networks. β-lactoglobulin fibril/polyacrylamide (PAAm) double network (DN) hydrogels were prepared using a one-pot method. The 2 wt% fibril solution was firstly concentrated by air flow. The weight of evaporated water was the total mass of other components added in fibril solution, in the final, fibril 2 wt%, TEOS 0.33 M (i.e., SiO_2 2 wt%), AAm 16 wt%, MBA 0.016 wt% and UV-initiator 0.8 wt%. The mixture was vortexed 3min and shacked 6h to obtain a homogeneous dispersion. 1.2 mL and 3 mL of this dispersion were transferred into modified syringe tubes respectively for the compressive and tensile tests, and then incubated at room temperature with the formation of silicified fibril network (first network). Next, the samples were placed under a UV lamp (wavelength 365 nm and intensity 11 watt) to carry out the photo-polymerization of AAm with the forming of PAAm network (second network). Finally, the DN hydrogels were removed from syringes for mechanical tests. The fibril and PAAm singe network (SN) hydrogels were prepared as the controls, the contents of fibril and PAAm in SN were kept the same as those in DN.

Characterization of amyloid fibrils and silicified fibrils. Electrophoretic mobilities of amyloid fibrils and silica were determined by the Zetasizer Nano ZS DLS device (Malvern Instruments).

Samples were inserted in the disposable folded capillary cells (DTS1070). Colloidal particle motion was measured by laser light scattering in a pulsed electric field, which is a function of electric field strength, dielectric constant and viscosity of the media, and the electrophoretic mobility of the particle.

Tapping mode atomic force microscopy (AFM) was carried out on a MultiMode VIII Scanning Force Microscope (Bruker) under ambient conditions using the AFM cantilevers (Bruker) with a vibrating frequency of 150 kHz. The microscope was covered with an acoustic hood to minimize vibrational noise. For sample preparations, 20 μL aliquots were deposited onto freshly cleaved mica, incubated for 2 min, rinsed with 1 mL of Milli-Q water and dried by pressured air. Images were simply flattened using the NanoScope Analysis 1.5 software, and no further image processing was carried out. The height profiles were plotted by exporting XZ data on height images using NanoScope Analysis 1.5 software.

Peak force quantitative nanomechanical (PF QNM) AFM was operated in intermittent mode under ambient conditions at a scan rate of 1 Hz. The AFM cantilevers (Bruker) were calibrated on the calibration samples – low-density polyethylene and polystyrene – covering the following ranges of Young's moduli: from 100 MPa to 2 GPa (for low-density polyethylene) and from 1 to 20 GPa (for polystyrene). The analysis of the Derjaguin–Mueller–Toporov (DMT) modulus was performed by the software Nanoscope Analysis.

Transmission electron microscopy (TEM) was used to characterize fibril-silica core-shell structures exploiting the electron density difference in silica and fibril. 5 μL of the dispersion, without staining, was deposited on copper grids covered with a carbon layer (Electron Microscopy Sciences) for 60s and then drained and washed twice with MilliQ water. The images were taken by bright-field TEM (FEI, Morgagni 268) operated at an acceleration voltage of 100 kV.

Small angle X-ray scattering (SAXS) experiments were performed using a Rigaku MicroMax-002+ microfocused beam source. The equipment has the microfocus X-ray source with a sealed tube Cu Kα (λ=1.542 Å), the applied voltage and filament current are 45 kV and 0.88 mA, respectively. The beam is collimated by three pinhole (0.4, 0.3, and 0.8 mm) collimators, and the scattering data were collected by a two-dimensional argon-filled detector. For sample preparation, 0.1 wt% fibril solutions with different silica contents were transferred into 1.5 mm quartz X-ray capillaries. The averaged scattered intensities versus the scattering vector q, with $q = \frac{4\pi}{\lambda} sin\frac{\theta}{2}$ (where θ is the scattering angle), were fitted by the polydisperse core-shell cylinder model.

Fourier transform infrared spectroscopy (FTIR) was used to characterize the interaction between fibril and silica and to identify the form of condensed silica. FTIR experiments were carried out by a Varian 640 spectrometer equipped with a Golden Gate diamond ATR stage. Samples were scanned over the range from 4000 to 400 cm^{-1} with a resolution of 2 cm^{-1} at room temperature and averaged over 64 scans.

Rheological Characterization. The viscoelastic properties of hydrogels were investigated by a rheometer (AR 2000, TA Instruments) with a geometry of 40 mm standard steel parallel plate and a gap distance of 500 μm. Dynamic strain (0.1-1000% strain, 1 Hz frequency) and frequency (0.1-100 Hz frequency, 1% strain) sweeps were performed to establish the linear viscoelastic region and the

frequency response of the samples, respectively. The network elasticity G_0 was chosen from the elastic modulus at a frequency of 1Hz. To investigate the network recovery properties, a high-magnitude strain (1000%) was applied to break the hydrogel network structure and a low-magnitude strain (1%) was applied to inspect the recovery of the hydrogel structure. The elasticity recovery rate was defined by the ratio of the recovery elasticity after the first destruction and heal cycle G_1 and its initial elasticity G_0. Solvent-trap was used to prevent the evaporation of solvent in all measurements.

Double network mechanical tests. Compressive tests were carried out using a TA.XT Plus Texture Analyzer (Stable Micro Systems) at a rate of 50 mm/min. The cylindrical samples with a height of 10 mm and a diameter of 12.5 mm were used. The compressive strain was estimated as h/h_0, where h is the height under compression and h_0 is the original height. Tensile tests were performed on Shimadzu Autograph AGS-X at a rate of 50 mm/min. The cylindrical samples with a height of 40 mm and a diameter of 9.6 mm were used. Both ends of the samples were gripped by the clamps with the clamp distance 10 mm. The stretch ratio λ was defined as the final length l divided by the original length l_0 of the specimen, $\lambda = l/l_0$. The Young's modulus was extracted from the slope of the stress−stretch curve at the linear region ($\lambda \approx 1.1-1.3$). The compressive modulus was extracted from the slope of the stress-strain curve at the linear region (strain ≤ 10%).

Aerogel characterization. Scanning Electron Microscopy (SEM) was performed using a Leo 1530 Gemini microscope (Zeiss) at 1kV acceleration voltage and a working distance of 5–6 mm. The in-lens detector was used and the samples were sputter coated with a layer of platinum prior to imaging.

The composition of fibril-silica composites were investigated by thermogravimetric analysis (TGA, Mettler Toledo). Prior to the measurements the samples were kept at 100 ^{o}C for 30 min to eliminate adsorbed water. Subsequently, the samples were heated from 100 ^{o}C to 900 ^{o}C at a heating rate of 10 ^{o}C/min in 900 μL alumina crucibles under oxygen or nitrogen gas flow, respectively. At 900 ^{o}C the samples were maintained at isothermal conditions for 30 min to estimate the silica content.

Nitrogen gas absorption-desorption experiments were performed to determine the specific surface area of aerogels (Micromeritics, Tristar 3000). Prior to measurements the samples were degassed for 2 h at 100 °C under a continuous nitrogen flow and the experiment data were recorded at 20 ^{o}C. The surface area is estimated by the Brunauer-Emmett-Teller (BET) method and the pore size distribution is extracted from the gas desorption curve.

Figures S1-S15

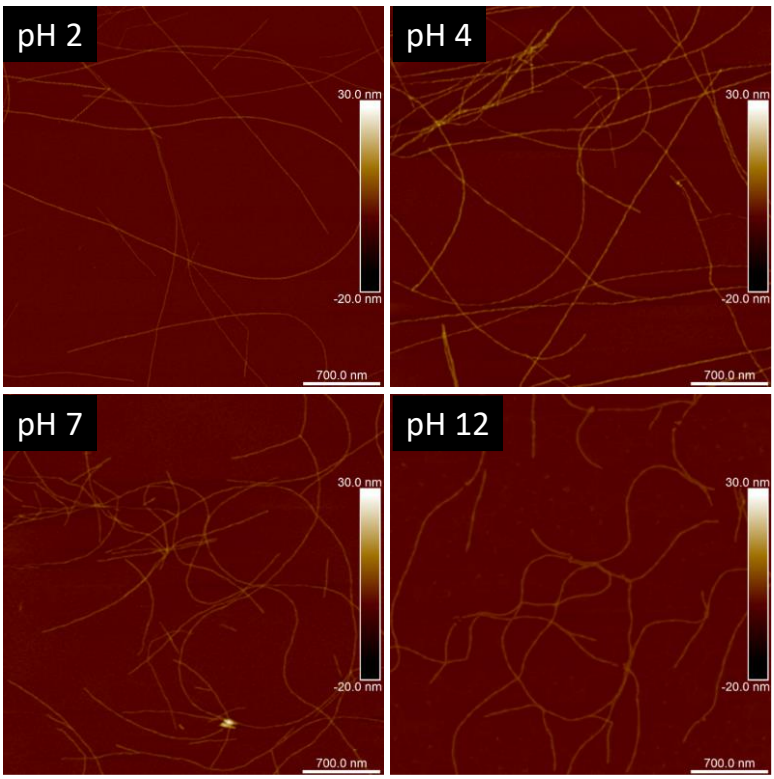

Figure S1. AFM images of the β-lactoglobulin amyloid fibrils at different pHs. The fibrils at pH 4, 7 and 12 were obtained by adjusting the pH of the mature fibrils (pH=2) using 2M NaOH.

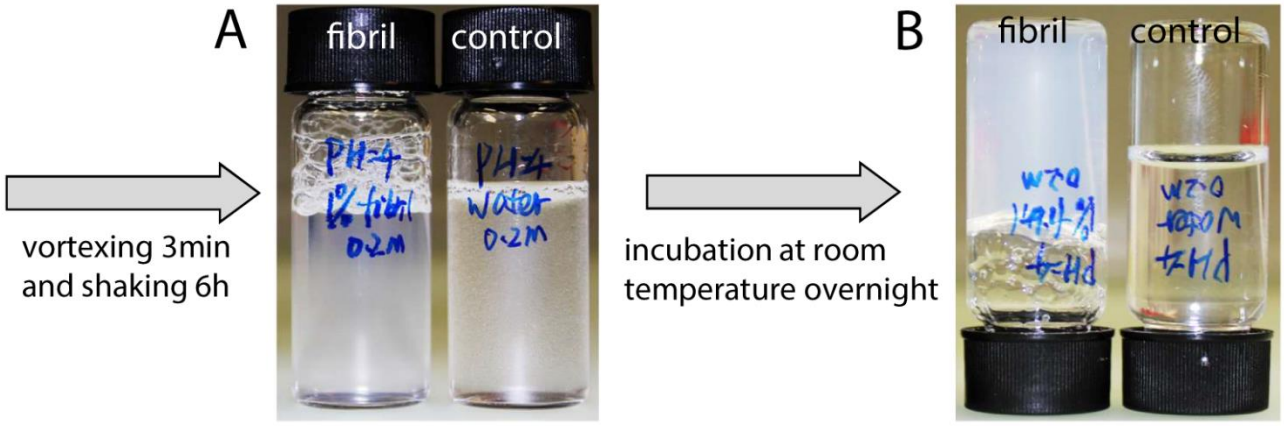

Figure S2. (A) Photos of the silica precursor TEOS in 1.0 wt% fibril solution (fibril) and Milli-Q water (control) after vortexing and shaking. TEOS = 0.2 M and pH = 4. It shows that the oil-like TEOS dissolves (hydrolyzes) in fibril solution rather than in Milli-Q water. (B) Photos of these samples after incubation overnight. The opaque self-supporting hydrogel is observed in the fibril system. This suggests that the condensation of silica is accelerated by the presence of fibrils, and the condensed silica plays a cross-linker role in hydrogels.

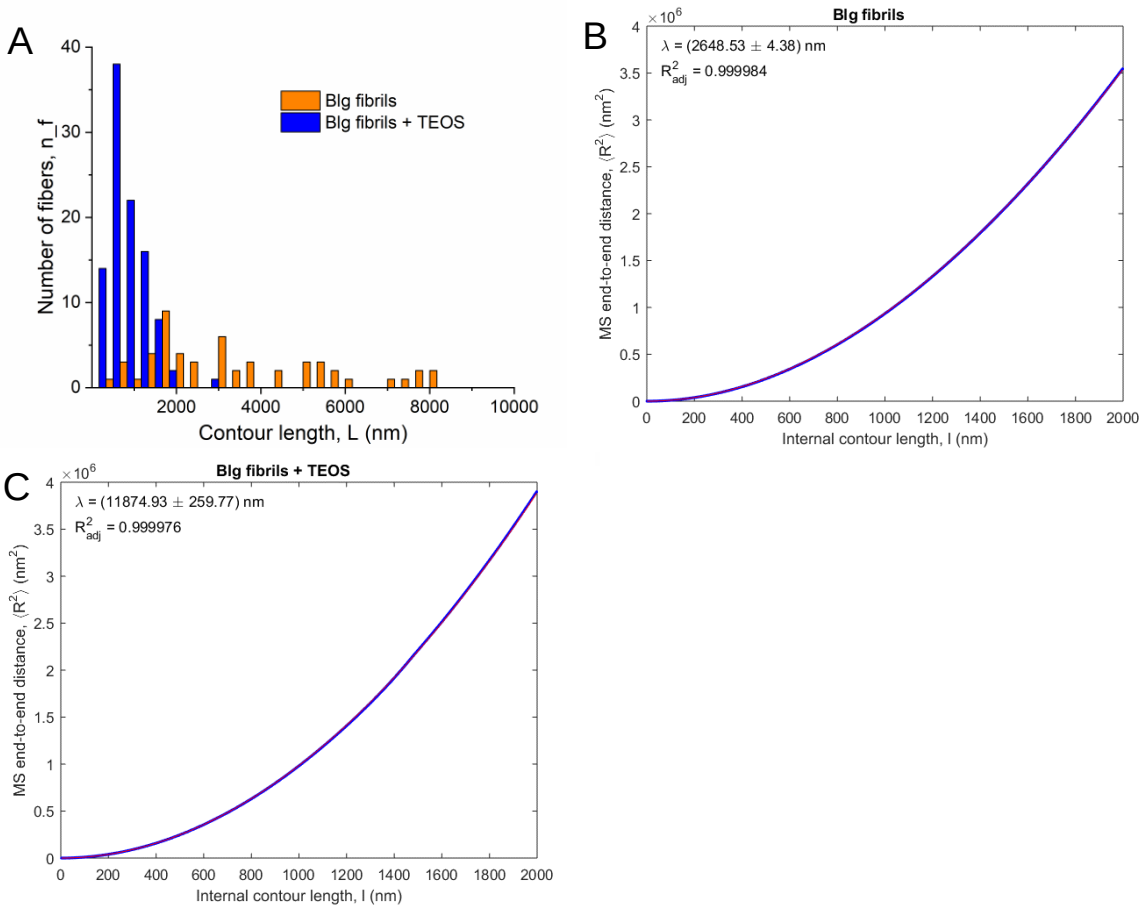

Figure S3. (A) Contour length distributions of amyloid fibrils (Blg fibrils) and silicified fibrils (Blg fibrils + TEOS). Plot of mean-squared end-to-end distance versus internal contour length for the amyloid fibrils (B) and silicified fibrils (C). The estimation of the persistence length was obtained by fitting the experimental data with the 2D worm-like chain model, yielding 2648 nm and 11874 nm for bare and silicified fibrils, respectively.

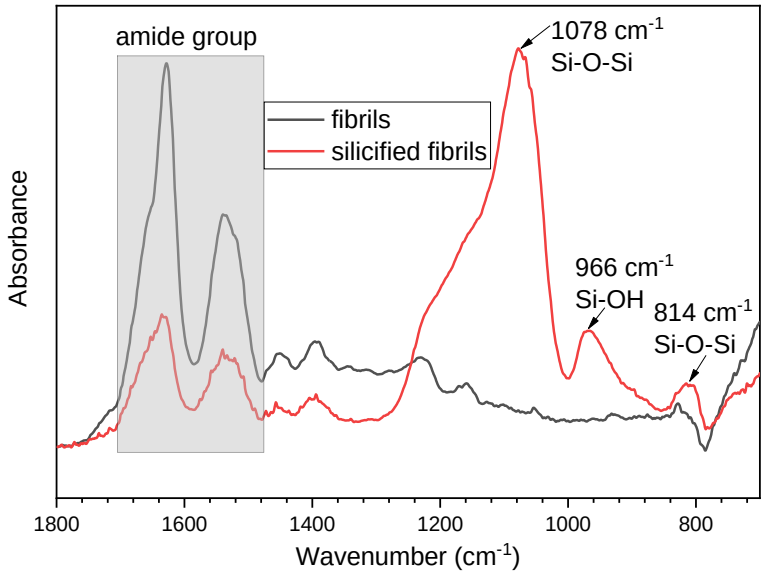

Figure S4. FTIR spectra of fibrils and silicified fibrils. The weaker amide group signal for silicified fibrils suggests the interactions between amyloid fibril and silica, i.e., that the amyloid fibrils were successfully coated by silica. The main composition of the silica in the shell is in the form of Si-O-Si.

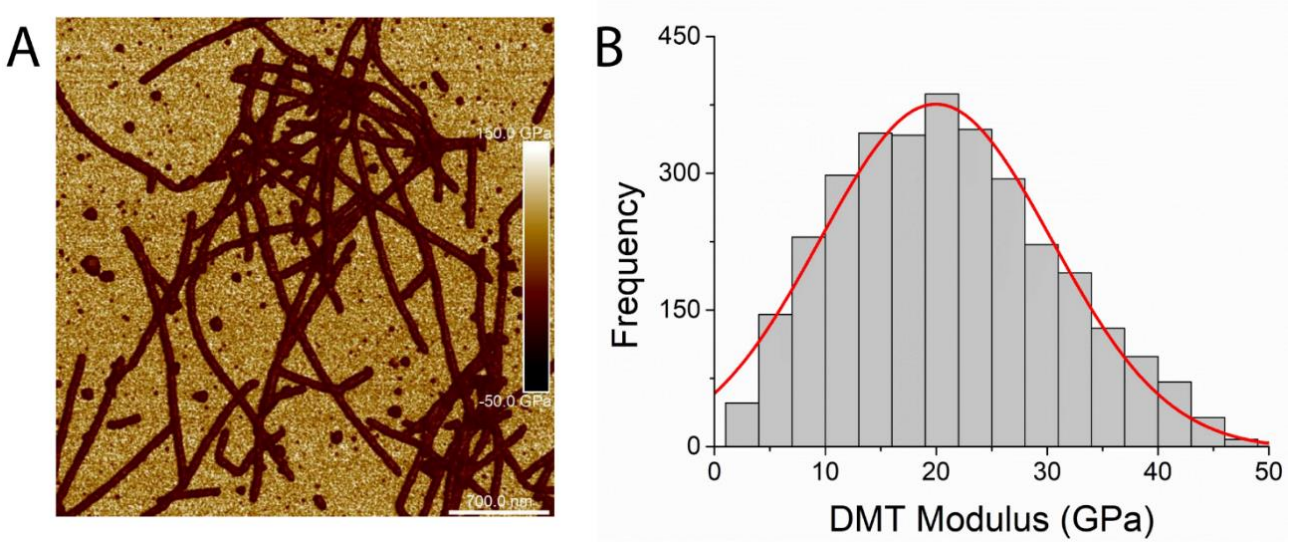

Figure S5. Young's modulus of the silicified β-lactoglobulin fibrils measured by PF QNM model: (A) DMT AFM image and (B) Young's modulus distribution. The β-lactoglobulin fibril and TEOS concentrations are 0.1wt% and 20 mM, respectively. The system pH is 4.

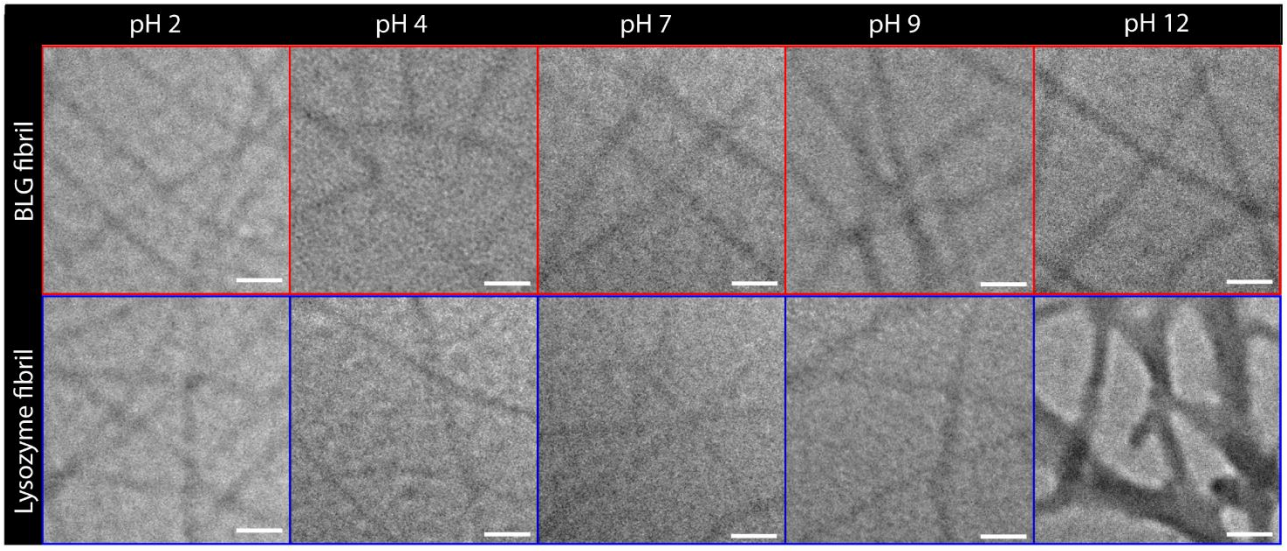

Figure S6. TEM images of the β-lactoglobulin fibril and lysozyme fibril at different pHs. The fibril concentrations are 0.1 wt% in each case. Scale bars are 50 nm.

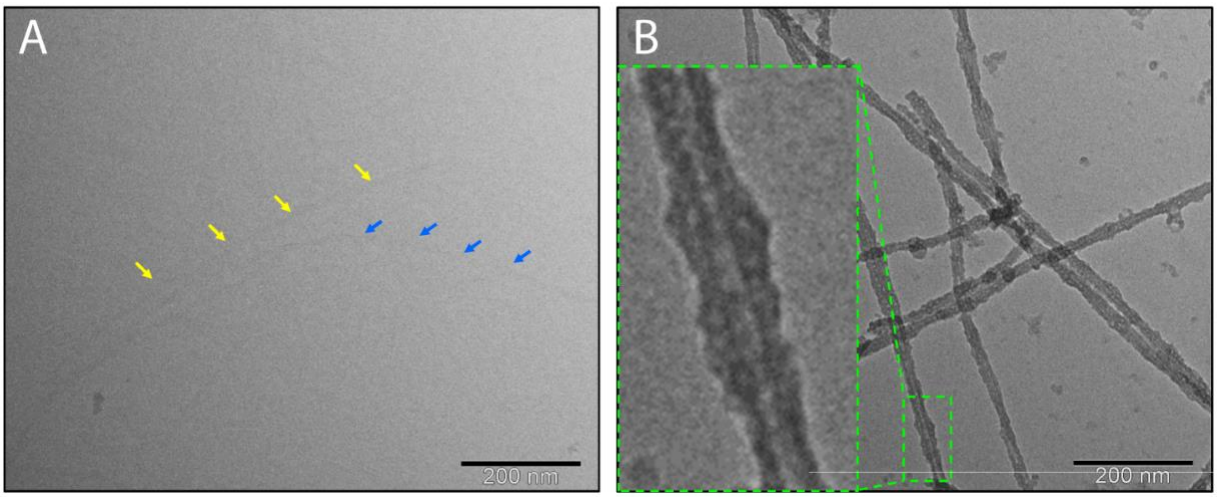

Figure S7. One example of the TEM contrast images of (A) lysozyme fibrils and (B) fibril-silica core-shell filaments. These two images were taken at identical instrumental conditions. This displays the electron contrast between fibril core and silica shell.

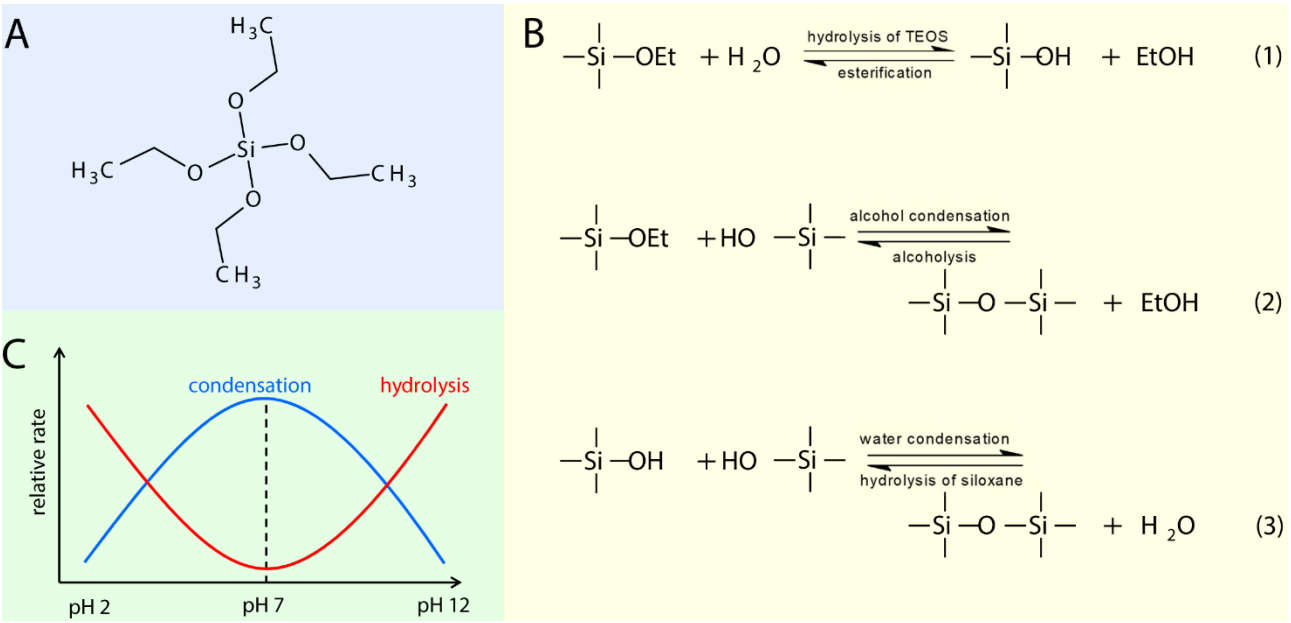

Figure S8. (A) Chemical structure of tetraethyl orthosilicate (TEOS). (B) Hydrolysis and condensation processes of TEOS. (C) Relative hydrolysis and condensation rates of TEOS at different pHs, where the H^+ and OH^- ions play the catalytic roles.

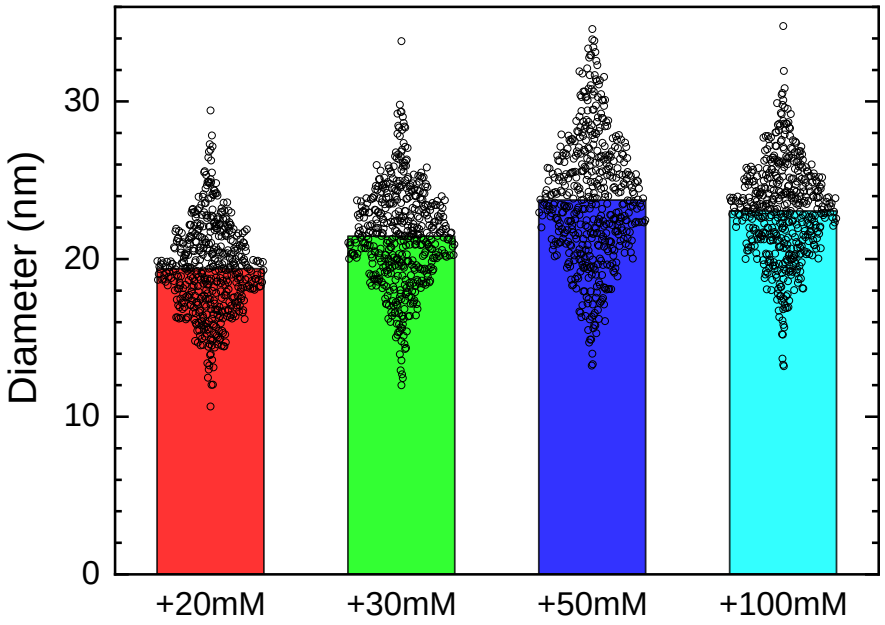

Figure S9. Diameter distribution of the silicified fibrils at different TEOS concentrations, obtained from analyzing the TEM images by the software ImageJ.

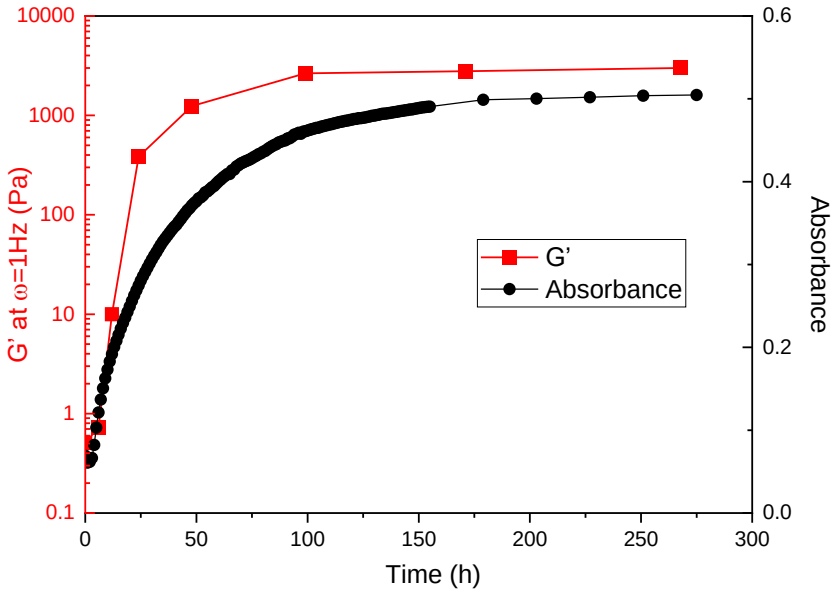

Figure S10. The evolution of silification process as monitored by UV-vis spectrometry at λ=600nm and rheological measurement for the sample 1wt% fibril + 0.2M TEOS.

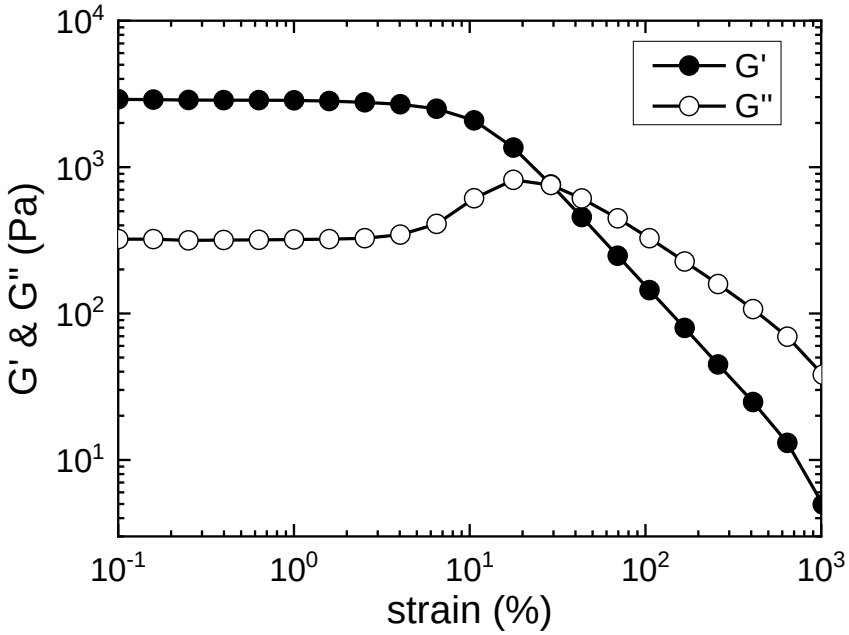

Figure S11. Strain sweep of the 1.0 wt% fibril+1.2 wt% SiO_2 hydrogel at a frequency of 1Hz. This shows that the hydrogel is in the linear region at a strain of 1% and broken at a strain of 1000%.

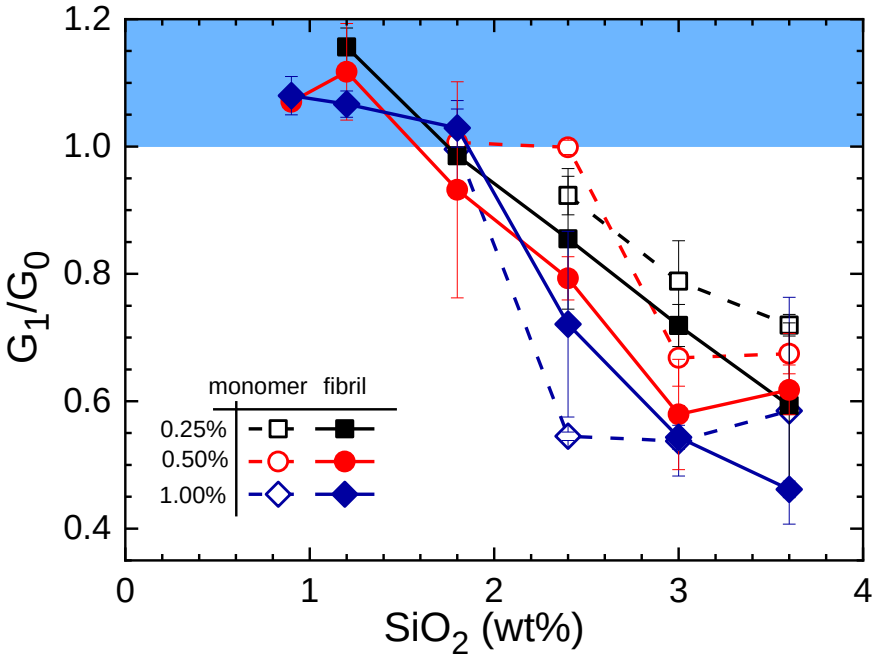

Figure S12. The elasticity recovery properties of fibril-silica hydrogels and protein-silica hydrogels at different fibril/protein and silica contents. The elasticity recovery rate G_1/G_0 is defined as the elasticity of hydrogel after first recovery G_1 over its initial elasticity G_0.

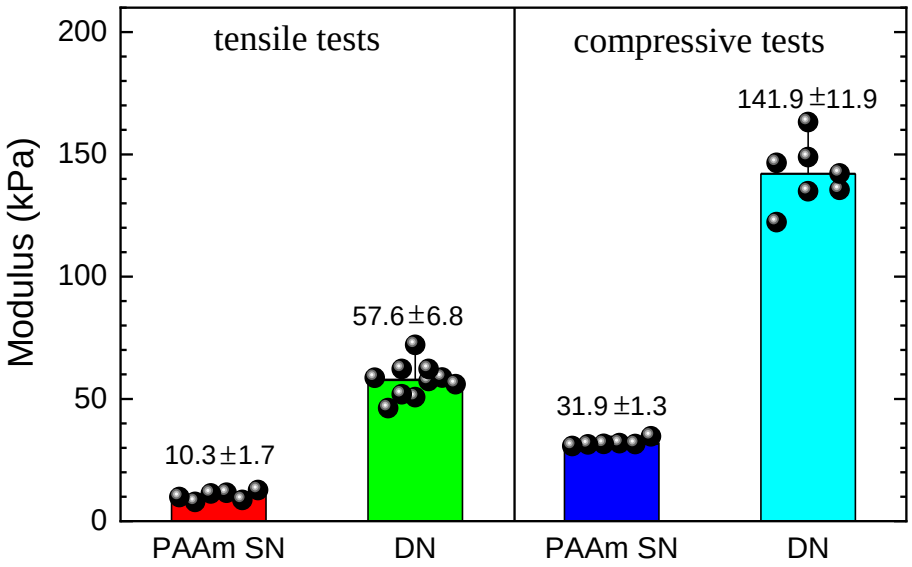

Figure S13. Left: Young's Moduli of PAAm SN and fibril/PAAm DN hydrogels obtained from tensile tests. Right: Compressive Moduli of hydrogels obtained from compressive tests.

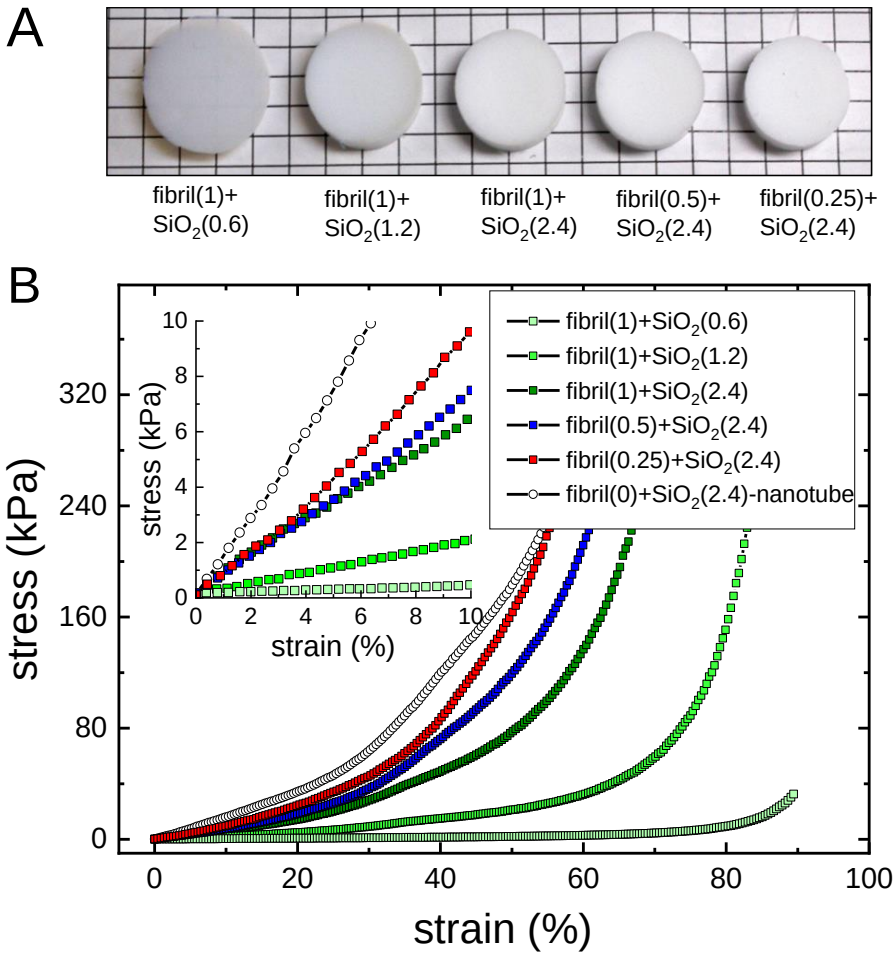

Figure S14. (A) Photo of the silicified fibril aerogels at different fibril and silica contents. The displayed contents of fibril and silica are the weight concentrations of fibril and silica in hydrogel state. For instance, fibril (1) + SiO_2 (0.6) aerogel is prepared from 1wt%fibril+0.6wt%SiO_2 hydrogel. (B) Strain-stress curves of silicified fibril aerogels in Panel A and silica nanotube aerogel in Figure 4C under uniaxial compression. The inserted figure shows the linear region, which is applied to calculate the compressive modulus as displayed in Table S2.

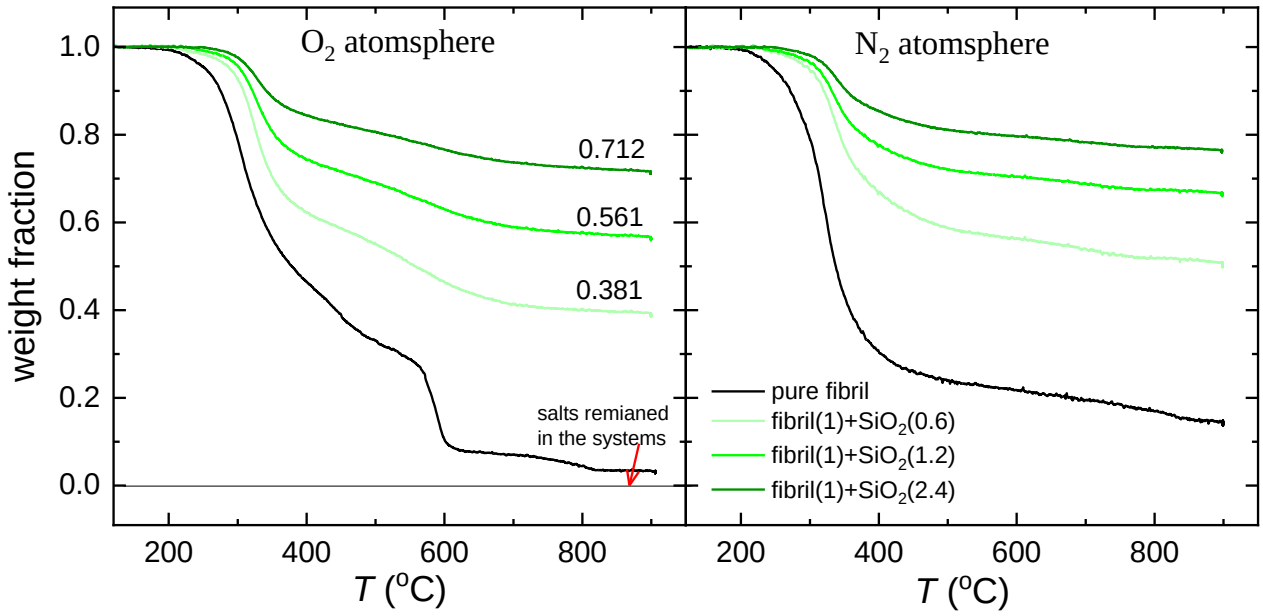

Figure S15. TGA curves of pure fibril and silicified fibrils in oxygen and nitrogen atmospheres, respectively. The theoretical SiO_2 contents are extremely close to the experimental inorganic contents ($\frac{0.6}{1+0.6} = 0.375 \cong 0.381$, $\frac{1.2}{1+1.2} = 0.545 \cong 0.561$, $\frac{2.4}{1+2.4} = 0.706 \cong 0.712$), illustrating the full condensation of TEOS. Otherwise, the un-hydrolyzed and un-condensed silica will diffuse into ethanol during the aerogel preparation. Note that the experimental values slightly higher than theoretical values is due to the salt introduced to the systems during pH adjustment from pH 2 to pH 4, as manifested by the pure fibril curve in O_2 atmosphere.

Tables S1-S2

Table S1. Fitting parameters of the fibril-silica core-shell structures.

	0.1wt% fibril +20mM TEOS	0.1wt% fibril +30mM TEOS	0.1wt% fibril +50mM TEOS
Scale	0.0007	0.00095	0.002
mean core radius (Å)	22	25	28
radial polydispersity (sigma)	0.6	0.55	0.6
core length (Å)	10000	10000	10000
radial shell thickness (Å)	68.1	78.5	88
face shell thickness (Å)	10	10	70
SLD core ($Å^{-2}$)	4.00E-06	4.00E-06	4.00E-06
SLD shell ($Å^{-2}$)	1.00E-06	1.00E-06	1.00E-06
SLD solvent ($Å^{-2}$)	4.00E-06	4.00E-06	4.00E-06
incoh. bkg (cm^{-1})	0.008	0.01	0.023

Table S2. Density, compressive modulus, and burn temperature of aerogels.

	density (g/L)	compressive modulus (kPa)	burn temperature (5% organic component loss) (°C)	burn temperature (10% organic component loss) (°C)
fibril	/	/	252.5	273.9
fibril(1)+SiO_2(0.6)	13.2	2.73	273.0	295.5
fibril(1)+SiO_2(1.2)	22.7	19.3	281.2	300.3
fibril(1)+SiO_2(2.4)	41.5	60.7	287.9	303.9
fibril(0.5)+SiO_2(2.4)	36.7	74.2	/	/
fibril(0.25)+SiO_2(2.4)	35.6	97.6	/	/
SiO_2(2.4)-nanotube	39.8	163	/	/

Appendix I: Calculation of the elasticity change during filament bundling

The elasticity of the network built from rigid filaments is $G \sim \kappa^2/\xi^5$ (see main text), thus only mesh size ξ and bending rigidity κ are considered in the following calculations. In the bundled network, we define m as the maximum number of virgin filaments in one bundled filament, $m \in [2, \infty)$, and i is the number of virgin filaments in the bundled filaments, $i \in [2, m]$.

Case I (m=2): Each bundled filament is only with two virgin filaments. Assume p is the probability of a bundling event, that is, in the present case, also the probability finding i =2 filaments, thus that the probability of finding virgin filaments is 1-p. In this case, $p \in [0,1]$. The change of the network structure can be described in Scheme S1.

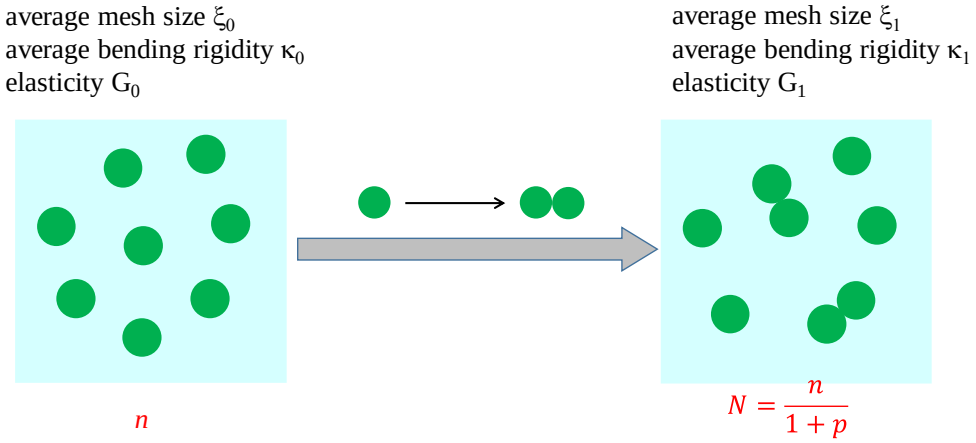

Scheme S1. Two-dimensional schematic illustration of the network structure before and after the filament bundles. Here each bundled filament is only with two virgin filaments. The probability of finding virgin filaments and i =2 filaments are 1-p and p, respectively. n and N represent the total number of filament before and after the bundling, respectively.

In the bundled network, as the mass balance, $N(1-p)\times 1 + Np \times 2 = n$, thus the total number of bundles (including the virgin filament) is $N = \frac{n}{1+p}$, i.e., $\frac{N}{n} = \frac{1}{1+p}$.

1. **Mesh size.** (a) According to the reference (4), for rigid rod network $\xi \sim (\sum L)^{-1/2}$, here $\sum L$ is the total contour length per unit volume, thus

$$\frac{\xi_1}{\xi_0} = \sqrt{\frac{n}{N}} = \sqrt{1+p}$$

(b) Or according to the reference (5), $\xi = \left(\frac{3\pi\rho d^2}{4c}\right)^{1/2}$, here ρ is the mass density of the filament, d is the diameter of filament, and c is the filament concentration in the network. For network 0, $\xi_0 = \left(\frac{3\pi\rho d^2}{4c}\right)^{1/2}$. For network 1, $\xi_1 = \left[\frac{3\pi\rho d^2[1\times(1-p)+2\times p]}{4c}\right]^{1/2} = \left[\frac{3\pi\rho d^2(1+p)}{4c}\right]^{1/2}$.

Again,

$$\frac{\xi_1}{\xi_0} = \sqrt{1+p} \tag{S1}$$

2. **Bending rigidity.** $\kappa = EI$, E is the Young's modulus and I is the area moment of inertia. According to the reference (6), the average area moment of inertia of ●● is $\langle I \rangle \approx m^2 I = 4I$, I is the area moment of inertia of ●.

$$\frac{\kappa_1}{\kappa_0} = \frac{I_1}{I_0} = \frac{I\times N(1-p)+4I\times Np}{I\times n} = \frac{N}{n}(1+3p) = \frac{1+3p}{1+p} \tag{S2}$$

Hence, the elasticity ratio, defined by the ratio of the network elasticity after and before filament bundles, is

$$\frac{G_1}{G_0} = \left(\frac{\kappa_1}{\kappa_0}\right)^2 \left(\frac{\xi_0}{\xi_1}\right)^5 = \frac{(1+3p)^2}{(1+p)^{9/2}}$$

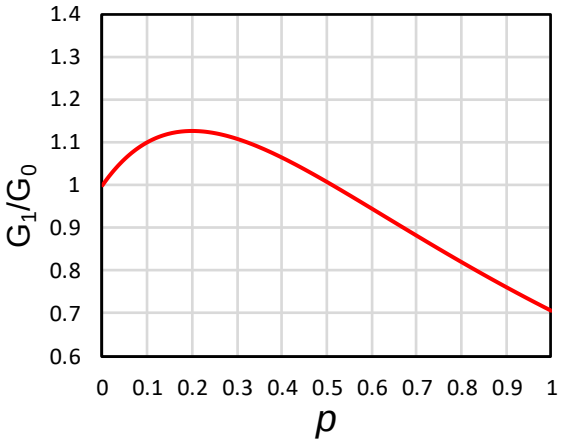

Figure S16. The elasticity change as a function of p. Here each bundled filament is only with two virgin filaments.

As shown in the Figure S16, the change of network elasticity shows two steps with increasing p. In first step ($p < 0.20$), the network elasticity increases, beyond that the elasticity decreases. From equations (S1) and (S2), we know both mesh size and bending rigidity increased with raising probability p, i.e., increasing the bundling content. The calculation displays that the increase in the filament bending rigidity is the dominating effect in the first step, while in the second step, the increase in the mesh size takes over. Importantly, the increase in elasticity predicted by this model is

closely matching the experimentally observed increase (see Figure 3E). This provides a quantified tool to model the change of network elasticity upon bundling.

Although we believe the case above is the most frequently observed experimentally, below we extend the treatment to the more general case where m>2, providing a general model of broad applicability.

Case II (m=3): Each bundled filament is with two or three virgin filaments, and assume that the probability of finding i =2 filaments and i =3 filaments are p and p^2, respectively. Thus the probability of finding virgin filaments is $1-p-p^2$. From $1-p-p^2 \geq 0$, we can deduce $p \in [0,0.614]$

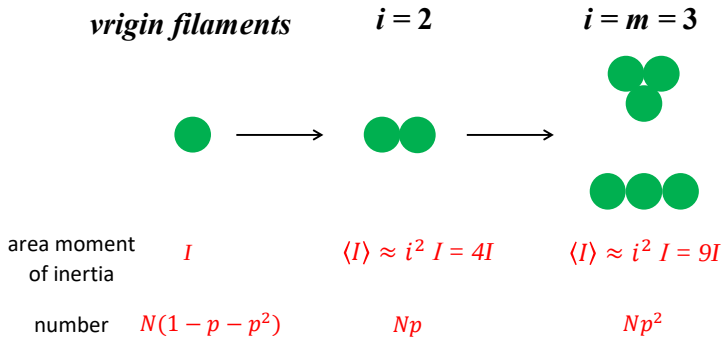

Scheme S2. Schematic illustration of the filament bundled process. Here each bundled filament is with two or three virgin filaments.

Based on the mass balance, $N(1-p-p^2)\times 1 + Np \times 2 + Np^2 \times 3 = n$, thus $\frac{N}{n} = \frac{1}{1+p+2p^2}$.

1. **Mesh size.** The mesh size ratio is
$$\frac{\xi_1}{\xi_0} = \sqrt{\frac{n}{N}} = \sqrt{1+p+2p^2}$$
2. **Bending rigidity.** As shown in Scheme S2, the bundled filaments with three virgin filaments have two cases, i.e. laterally arranged and closely packaged. For laterally arranged filaments, the average area moment of inertia $\langle I\rangle = i^2 I\sqrt{\frac{4}{3}-\frac{1}{3i^2}} \approx i^2 I$ (6). For closely packed filaments, the bundled filament radius is $R \approx \sqrt{\frac{i\pi r^2}{\pi}} = \sqrt{i}r$, thus $\langle I\rangle \approx \frac{\pi R^4}{4} = \frac{i^2\pi r^4}{4} = i^2 I$. These mean that the average area moments of inertia for both laterally arranged and closely packaged filaments can be approximated to $i^2 I$.

Thus bending rigidity ratio is
$$\frac{\kappa_1}{\kappa_0} = \frac{I_1}{I_0} = \frac{I\times N(1-p-p^2) + 4I \times Np + 9I \times Np^2}{I \times n} = \frac{1+3p+8p^2}{1+p+2p^2}$$
Hence, the elasticity ratio is:
$$\frac{G_1}{G_0} = \left(\frac{\kappa_1}{\kappa_0}\right)^2 \left(\frac{\xi_0}{\xi_1}\right)^5 = \frac{(1+3p+8p^2)^2}{(1+p+2p^2)^{9/2}}$$

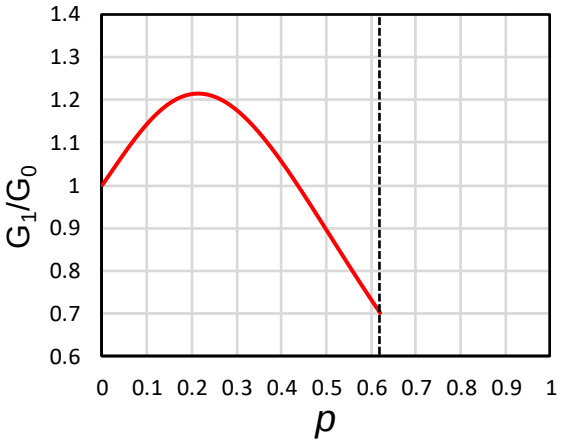

Figure S17. The elasticity change as a function of *p*. Here each bundled filament is only with two or three virgin filaments. The plotting stops at p=0.614 to compel with the requirement of all probabilities ≥ 0.

As displayed in Figure S17, the elasticity change tendency is similar to the case I, the elasticity first increases with raising *p* and then decreases. The boundary for these two steps is at p = 0.21 and the recovery ratio around 1.21.

Case III (m=m and ∞): Each bundled filament can be with two, three, …, or *m* virgin filaments. Assume that the probability of finding *i* filaments is p^{i-1}. Thus the probability of finding virgin filaments is:

$$1 - p - p^2 - \cdots - p^{m-1} - p^m = 1 - \sum_{i=2}^{m} p^{i-1}$$

In this case, $p \in [0,0.5]$.

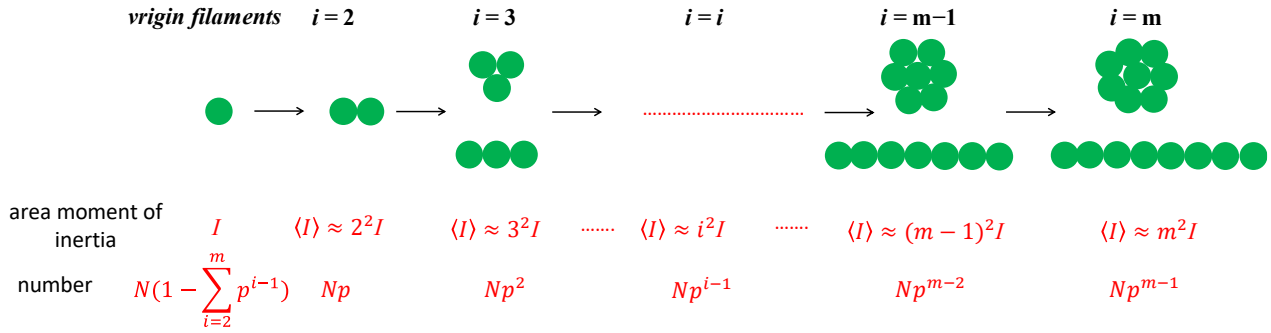

Scheme S3. Schematic illustration of the filament bundled process. Here each bundled filament is with two, three, …, or *m* virgin filaments.

Based on the mass balance,

$$N\left(1 - \sum_{i=2}^{m} p^{i-1}\right) \times 1 + Np \times 2 + Np^2 \times 3 + \cdots + Np^{m-2} \times (m-1) + Np^{m-1} \times m = n$$

thus

$$\frac{n}{N} = 1 + \sum_{i=2}^{m} (i-1) p^{i-1}$$

The mesh size ratio is,

$$\frac{\xi_1}{\xi_0} = \sqrt{\frac{n}{N}} = \sqrt{1 + \sum_{i=2}^{m} (i-1)p^{i-1}}$$

Thus bending rigidity ratio is

$$\frac{\kappa_1}{\kappa_0} = \frac{I \times N(1 - \sum_{i=2}^{m} p^{i-1}) + 2^2 I \times Np + 3^2 I \times Np^2 + \cdots i^2 I \times Np^{i-1} \ldots + (m-1)^2 I \times Np^{m-2} + m^2 I \times Np^{m-1}}{I \times n}$$

$$= \frac{1 + \sum_{i=2}^{m} (i^2 - 1)p^{i-1}}{1 + \sum_{i=2}^{m} (i-1)p^{i-1}}$$

Hence, the elasticity ratio for *m*=*m* is

$$\frac{G_1}{G_0} = \left(\frac{\kappa_1}{\kappa_0}\right)^2 \left(\frac{\xi_0}{\xi_1}\right)^5 = \frac{\left[1 + \sum_{i=2}^{m} (i^2 - 1)p^{i-1}\right]^2}{\left[1 + \sum_{i=2}^{m} (i-1)p^{i-1}\right]^{\frac{9}{2}}}$$

$$= \frac{[1 + 2p^2 - p^3 - m(m+2)p^m + (2m^2 + 2m - 3)p^{m+1} - (m^2 - 1)p^{m+2}]^2 (1-p)^3}{[1 - p + p^2 - mp^m + (m-1)p^{m+1}]^{9/2}}$$

the elasticity ratio for *m*= ∞ is

$$\frac{G_1}{G_0} = \frac{(1 + 2p^2 - p^3)^2 (1-p)^3}{(1 - p + p^2)^{9/2}}$$

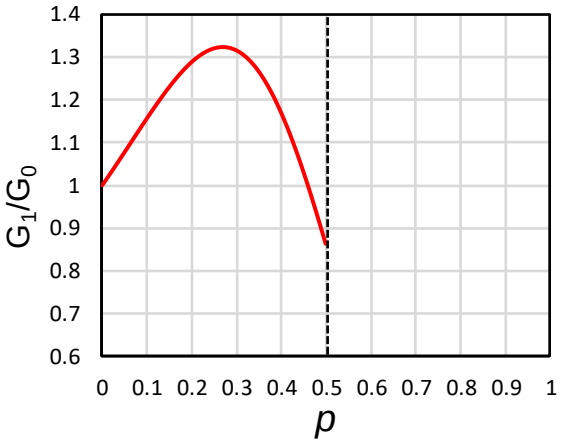

Figure S18. The elasticity change as a function of *p*. Here each bundled filament is with two, three, …… infinite virgin filaments. The plotting stops at *p*=0.5 is the requirement for all probabilities ≥ 0.

As displayed in Figure S18, the elasticity change tendency shows a similar non-monotonic behavior as cases I and II, i.e., the elasticity first increases and then decreases with increasing *x*. Here the boundary value is *p* = 0.27 and the maximum recovery elasticity ratio just above 1.3.

Appendix II: Calculation of the surface area of fibril-silica core-shell structures

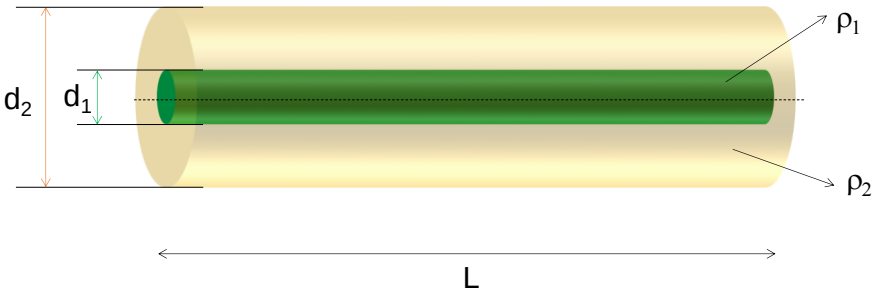

Scheme S4. Schematic illustration of the core-shell filament with the core diameter of d_1 and the shell thickness of $(d_2\text{-}d_1)/2$. The densities of core and shell are ρ_1 and ρ_2, respectively. L is filament length.

The total mass of the core-shell filament is $m = \frac{\pi d_1^2}{4} L\rho_1 + \frac{\pi(d_2^2-d_1^2)}{4} L\rho_2 = \frac{\pi d_1^2}{4} L(\rho_1 - \rho_2) + \frac{\pi d_2^2}{4} L\rho_2$, and the total surface is $S = \pi d_2 L$. Thus, the specific surface area can be written as $\frac{S}{m} = \frac{\pi d_2 L}{\frac{\pi d_1^2}{4} L(\rho_1-\rho_2)+\frac{\pi d_2^2}{4} L\rho_2} = \frac{4d_2}{d_1^2(\rho_1-\rho_2)+d_2^2\rho_2}$, which is independent of the filament length L.

In the BET surface area analysis experiment, the fibril(1)+SiO_2(2.4) aerogel is used, with an experimental result value of 648 m^2/g. The fibril core diameter is $d_1 \approx 5$ nm, core-shell filament diameter is $d_2 \approx 20$ nm (Figure 2C), and $\rho_1 = 1.3$ g/cm^3 (7).

1. Assume that the density of silica shell is ρ_2 = **2.65 g/cm^3** (SiO_2 solid) (8).

$$\frac{S}{m} = \frac{4d_2}{d_1^2(\rho_1-\rho_2) + d_2^2\rho_2} = \frac{4 \times 20}{5^2 \times (1.3 - 2.65) + 20^2 \times 2.65} \times \frac{nm}{nm^2 \times g \times cm^{-3}}$$
$$= 0.078 \times \frac{10^3 m^2}{g} = 78 m^2/g$$

2. A silica shell density ρ_2 = **0.208 g/cm^3** can deduced from the mass ratio of silica and fibril as suggested by TGA experiments.

$$\frac{silica}{fibril} = \frac{2.4}{1} = \frac{\frac{\pi(d_2^2-d_1^2)}{4} L\rho_2}{\frac{\pi d_1^2}{4} L\rho_1} \Longrightarrow\Longrightarrow\Longrightarrow \rho_2 = \frac{2.4 \times \rho_1 \times d_1^2}{d_2^2 - d_1^2} = 0.208\ g/cm^3 \ .$$

$$\frac{S}{m} = \frac{4d_2}{d_1^2(\rho_1-\rho_2) + d_2^2\rho_2} = \frac{4 \times 20}{5^2 \times (1.3 - 0.208) + 20^2 \times 0.208} \times \frac{10^3 m^2}{g} = 724\ m^2/g$$

Which is in perfect agreement with BET experiments.

References

1. Vigolo D, *et al.* (2017) Continuous isotropic-nematic transition in amyloid fibril suspensions driven by thermophoresis. *Scientific Reports* 7:1211.
2. Jung JM, Savin G, Pouzot M, Schmitt C, Mezzenga R (2008) Structure of heat-induced β-lactoglobulin aggregates and their complexes with sodium-dodecyl sulfate. *Biomacromolecules* 9(9):2477–2486.
3. Nystrom G, Fernandez-Ronco MP, Bolisetty S, Mazzotti M, & Mezzenga R (2016) Amyloid templated gold aerogels. *Advanced Materials* 28(3):472-478.
4. Salamon, K., Aumiler, D., Pabst, G., & Vuletic, T. (2013). Probing the mesh formed by the semirigid polyelectrolytes. *Macromolecules*, *46*(3), 1107-1118.
5. Schmidt, C. F., Baermann, M., Isenberg, G., & Sackmann, E. (1989). Chain dynamics, mesh size, and diffusive transport in networks of polymerized actin: a quasielastic light scattering and microfluorescence study. *Macromolecules*, *22*(9), 3638-3649.
6. Usov, I., & Mezzenga, R. (2014). Correlation between nanomechanics and polymorphic conformations in amyloid fibrils. *ACS Nano*, *8*(11), 11035-11041.
7. Nyström, G., Arcari, M., & Mezzenga, R. (2018). Confinement-induced liquid crystalline transitions in amyloid fibril cholesteric tactoids. *Nature Nanotechnology*, 13(4), 330.
8. Silicon dioxide (Wikipedia). https://en.wikipedia.org/wiki/Silicon_dioxide#cite_note-b92-1.